INTERNATIONAL JOURNAL FOR NUMERICAL METHODS IN FLUIDS
Int. J. Numer. Meth. Fluids 2009; **60**:27–53
Published online 6 August 2008 in Wiley InterScience (www.interscience.wiley.com). DOI: 10.1002/fld.1876

An efficient and accurate non-hydrostatic model with embedded Boussinesq-type like equations for surface wave modeling

Chih-Chieh Young[1] and Chin H. Wu[2,*,†]

[1]*Department of Civil Engineering, National Taiwan University, Taipei 10617, Taiwan*
[2]*Department of Civil and Environmental Engineering, University of Wisconsin, Madison, WI, U.S.A.*

SUMMARY

A novel approach that embeds the Boussinesq-type like equations into an implicit non-hydrostatic model (NHM) is developed. Instead of using an integration approach, Boussinesq-type like equations with a reference velocity under a virtual grid system are introduced to analytically obtain an analytical form of pressure distribution at the top layer. To determine the size of vertical layers in the model, a top-layer control technique is proposed and the reference location is employed to optimize linear wave dispersion property. The efficiency and accuracy of this NHM with Boussinesq-type like equations (NHM-BTE) are critically examined through four free-surface wave examples. Overall model results show that NHM-BTE using only two vertical layers is capable of accurately simulating highly dispersive wave motion and wave transformation over irregular bathymetry. Copyright © 2008 John Wiley & Sons, Ltd.

Received 2 January 2008; Accepted 2 June 2008

KEY WORDS: non-hydrostatic; implicit method; free-surface waves; Boussinesq-type like equations; reference velocity; pressure distribution

1. INTRODUCTION

Efficient and accurate modeling of surface wave motions plays an important role in many coastal and ocean engineering problems. For several decades, a great deal of efforts has been paid to develop unified models that can effectively predict water wave propagation with varying degree of dispersive and nonlinear effects [1, 2]. The Boussinesq-type wave equations, one kind of depth-integrated models, provide an efficient and accurate framework to model wave propagating from

*Correspondence to: Chin H. Wu, Department of Civil and Environmental Engineering, 1269D Engineering Hall, University of Wisconsin, Madison, WI 53706, U.S.A.
†E-mail: chinwu@engr.wisc.edu

Contract/grant sponsor: National Science Council of the Republic of China; contract/grant number: 096-2917-I-002-036
Contract/grant sponsor: NSF; contract/grant number: NSF-OCE-0628560

deep water to shallow water. The basic concept is to reduce the vertical coordinate by considering a certain degree of the non-hydrostatic effects (attributed to the vertical acceleration of fluids). For example, Peregrine [3] derived the conventional Boussinesq equations by integrating continuity equation and momentum equations over the water depth under the assumption of equal and weak nonlinearity and frequency dispersion. Continuous progress has been made to remove the original constraints to nonlinear (larger wave height) and shorter (deeper water depth) waves through the modified forms of Boussinesq-type equations [4–10]. Extensive review of this subject can refer to Dingemans [11], Madsen and Schäffer [12], and Kirby [13] and will not be discussed here. While the latest Boussinesq-type wave models are capable of simulating highly nonlinear and dispersive waves, several challenging issues, (i) assumptions of irrotational and inviscid flow; (ii) difficulties in describing vertical flow structure and wave breaking; and (iii) complexities and stabilities due to higher-order derivatives of mathematical equations and numerical schemes, have confront many researchers [14–17].

An alternative approach to tackle the above-challenging issues is to solve the three-dimensional (3D) Navier–Stokes equations (NSEs) that directly include the non-hydrostatic pressure in the vertical direction. There have been a great amount of efforts paid to develop accurate and efficient non-hydrostatic models (NHMs) for predicting wave propagating from deep water to shallow water. From the numerical algorithm viewpoint, methods to solve the NSE or NHM, in general, can be classified into three categories: (i) explicit projection methods [18–24], (ii) semi-implicit, fractional step methods [25–29], and (iii) fully implicit methods [30–33]. For explicit projection methods or semi-implicit methods, an iterative matrix solver is usually needed to solve the resulting pressure Poisson equation. On the other hand, fully implicit methods can discretize the NSE to yield a block tri-diagonal matrix system with the unknown horizontal velocity, which is directly solved without iteration.

In terms of modeling the moving free-surface, several methods have been successfully incorporated into the NHMs. In general, there are (i) marker and cell method [34, 35], (ii) volume of fluid method [36, 37], (iii) arbitrary Lagrangian–Eulerian method [38, 39], (iv) level-set method [40, 41], and (v) surface height method [42]. All these methods except for the last one is capable of tracking/capturing complicated free surfaces such as overturning/breaking waves but requires a relatively high computational expense. This is particularly demanding for 3D surface wave modeling. On the other hand, the surface wave height method obtains the free-surface elevation as a single-valued function of horizontal location and time. It has been demonstrated that NHMs using the surface height method is an effective method to simulate small-amplitude waves and steep non-overturning waves [19, 25–27, 32, 43, 44].

Accurately expressing the free-surface boundary condition in non-hydrostatic modeling has a great influence on capturing wave propagation [22, 32]. Previous studies show that NHMs with a hydrostatic pressure at the top layer require a relatively large number of vertical layers (10–20 cells) to satisfactorily simulate dispersive waves [20, 25–27, 29, 30]. To reduce the required number of vertical layers, Stelling and Zijlema [22] proposed a Keller-box scheme, an edged-based grid system in the vertical direction, so that the pressure boundary condition at the top layer can be exactly assigned without any approximation. Zijlema and Stelling [28] later employed the Keller-box scheme into their semi-implicit finite volume NHM. Recognizing most models based on a staggered grid system, Yuan and Wu [31, 32] proposed an integration method to successfully remove the top-layer hydrostatic pressure assumption. Subsequently, Choi and Wu [23] employed the integration method and Ahmadi *et al.* [45] proposed an interpolation approach, a similar concept like the integral approach but based on direct numerical discretization for the top-layer pressure, to their explicit projection-based non-hydrostatic model. Overall results from these models that

DOI: 10.1002/fld

consider the effects of non-hydrostatic pressure at the top layer indicate that only a small number of vertical layers (2–5 layers, an order of magnitude smaller than models without non-hydrostatic pressure) is needed for simulating nearshore wave transformation including shoaling, dispersion, refraction, and diffraction phenomena. Yuan and Wu [44] reported that the required number of vertical layers depends on a non-dimensional relative water depth Kh, where K and h are the wave number and water depth, respectively. It is also recognized that more vertical layers are required to resolve highly dispersive deep-water waves. For example, under a given error tolerance of 1% phase speed, a two-layer model is accurate up to $Kh=1$ while a five-layer model can resolve linear dispersion up to $Kh=5$. A so-called top-down resolving (TDR) technique was also suggested to determine a set of suitable thickness for each vertical layer.

In this study, a novel method that combines the Boussinesq-type like equations at the free surface and a NHM is developed and examined. Without imposing irrotational and inviscid flow assumptions, an analytical form of pressure distribution based on the Boussinesq-type like equations with a reference velocity is embedded into the NHM by Yuan and Wu [44]. In addition, a top-layer control (TLC) technique, instead of the TDR technique, is also proposed to optimize the linear wave dispersion property. Performance and comparison between the NHM with Boussinesq-type like equations (NHM-BTE) and NHM are illustrated through four free-surface wave examples. In the following, Section 2 presents the governing equations and the boundary conditions. Section 3 states the numerical methods including general discretization, the embedded Boussinesq-type like equations, and overall algorithm. In Section 4 four examples including sloshing waves and progressive waves over two-dimensional (2D) and 3D uneven bottom topography are used to examine the accuracy and efficiency of the model. Finally, summary and conclusions are given in Section 5.

2. GOVERNING EQUATIONS AND BOUNDARY CONDITIONS

For simulating free-surface flows, the governing equations are the unsteady, incompressible, 3D NSEs in a Cartesian coordinate system (x, y, z) and time t. Figure 1 shows a computational domain, which is vertically bounded between the bottom $z=-h(x, y)$ and the moving free surface $z=\eta(x, y, t)$, where the water depth $h(x, y)$ and the free-surface elevation $\eta(x, y, t)$ are measured from the undisturbed mean water level.

The governing equations that satisfy the conservation of mass and momentum are

$$\frac{\partial u}{\partial x}+\frac{\partial v}{\partial y}+\frac{\partial w}{\partial z}=0 \tag{1}$$

$$\frac{\partial u}{\partial t}+u\frac{\partial u}{\partial x}+v\frac{\partial u}{\partial y}+w\frac{\partial u}{\partial z}=-\frac{\partial P}{\partial x}+\nu\frac{\partial^2 u}{\partial x^2}+\nu\frac{\partial^2 u}{\partial y^2}+\nu\frac{\partial^2 u}{\partial z^2} \tag{2}$$

$$\frac{\partial v}{\partial t}+u\frac{\partial v}{\partial x}+v\frac{\partial v}{\partial y}+w\frac{\partial v}{\partial z}=-\frac{\partial P}{\partial y}+\nu\frac{\partial^2 v}{\partial x^2}+\nu\frac{\partial^2 v}{\partial y^2}+\nu\frac{\partial^2 v}{\partial z^2} \tag{3}$$

$$\frac{\partial w}{\partial t}+u\frac{\partial w}{\partial x}+v\frac{\partial w}{\partial y}+w\frac{\partial w}{\partial z}=-\frac{\partial P}{\partial z}-g+\nu\frac{\partial^2 w}{\partial x^2}+\nu\frac{\partial^2 w}{\partial y^2}+\nu\frac{\partial^2 w}{\partial z^2} \tag{4}$$

where $u(x, y, z, t)$, $v(x, y, z, t)$, and $w(x, y, z, t)$ are the velocity components in the x, y, and z directions, respectively; $P(x, y, z, t)$ is the normalized pressure, i.e. pressure divided by a constant

DOI: 10.1002/fld

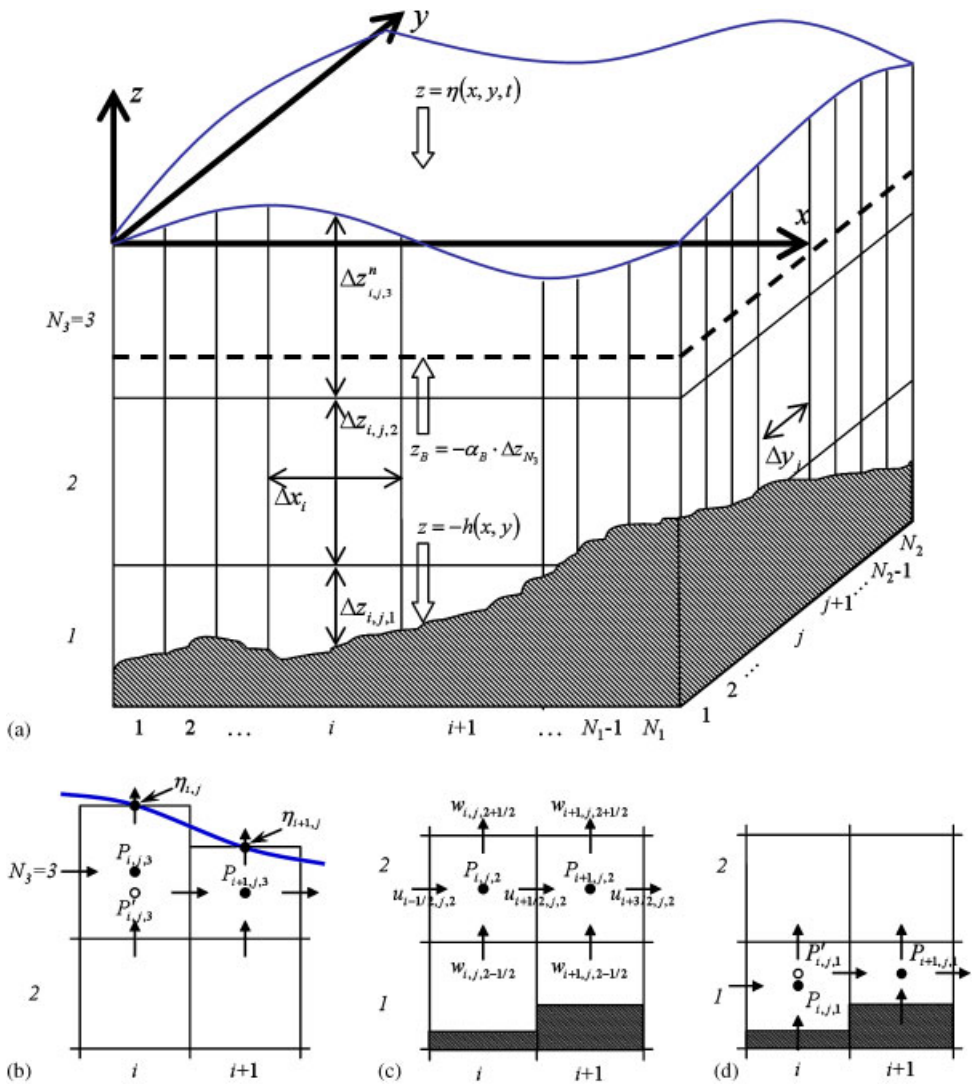

Figure 1. (a) A sketch of the computational domain (solid lines) and the virtual frame (dashed lines) under a Cartesian grid system, and staggered arrangements of variables at (b) free-surface cells, (c) interior cells, and (d) bottom cells.

reference density; g is the gravitational acceleration constant; and v is the kinematic viscosity and is zero for an inviscid fluid.

Various boundary conditions are used for modeling free-surface waves. The kinematic boundary conditions at the impermeable bottom and the free surface are

$$u\frac{\partial h}{\partial x}+v\frac{\partial h}{\partial y}+w\Big|_{z=-h}=0 \tag{5}$$

DOI: 10.1002/fld

and

$$\frac{\partial \eta}{\partial t}+u\frac{\partial \eta}{\partial x}+v\frac{\partial \eta}{\partial y}=w|_{z=\eta} \tag{6}$$

respectively. By integrating the continuity equation (1) over the water depth and applying Leibniz's rule with the kinematic boundary conditions (5) and (6), we obtain the conservative form of free-surface equation:

$$\frac{\partial \eta}{\partial t}+\frac{\partial}{\partial x}\int_{-h}^{\eta} u\,\mathrm{d}z+\frac{\partial}{\partial y}\int_{-h}^{\eta} v\,\mathrm{d}z=0 \tag{7}$$

In addition, the continuity of normal stress at the free surface is enforced, i.e. $P(x, y, \eta, t)=P_{\mathrm{a}}$, where P_{a} is the atmospheric pressure and taken as zero here. At the inflow boundary, the horizontal velocity component is specified by either analytical solutions or laboratory conditions. To avoid unwanted waves generated by impulse motions, we use a ramp-function, i.e.

$$\frac{1}{2}\left(1+\tanh\frac{t-2T}{T}\right)$$

where T is the wave period. At the outflow boundary, the combination of the Sommerfeld radiation boundary condition and a sponge layer technique [31, 35] is employed to minimize wave reflection into the computational domain.

3. NUMERICAL METHODS

In this paper, the Boussinesq-type like equations are embedded under a virtual grid framework system into a NHM [32]. Instead of using an integration method [32, 44], an interpolation method [19, 45], and a ghost cell approach [46], we employ the Boussinesq-type like equations to exactly describe the vertical pressure distribution using the non-hydrostatic velocity as the reference velocity. This new method provides an effective way to characterize the top layer pressure under the staggered grid system. In the following, general discretization of NHM is briefly described here and details of numerical algorithm can be referred to Yuan and Wu [32]. Subsequently, the development and implementation of the embedded Boussinesq-type like equations under the virtual grid system are presented in Section 3.2. Section 3.3 will summarize the overall algorithm of the model.

3.1. General discretization

The NHM is based on a Cartesian staggered grid system. Figure 1 shows the computational domain discretized by N_1, N_2, and N_3 cells in the x, y, and z directions with the grid indices i, j, and k, respectively. In the model a non-uniform grid spacing, Δx_i, Δy_j, and $\Delta z_{i,j,k}$ along each direction can be set. To delineate irregular bathymetries, an effective partial-cell method [47] is used. An implicit method is applied to discretize the governing equations, which would be presented in matrices next.

Continuity equation: After discretizing the continuity equation (1) from the bottom cell to the free-surface cell, the vertical velocity at the position $(i, j, k+\frac{1}{2})$, i.e. $w_{i,j,k+1/2}$, is related to the lower vertical velocity at the position $(i, j, k-\frac{1}{2})$, i.e. $w_{i,j,k-1/2}$, and its adjacent horizontal velocities. Applying the kinematic boundary condition (5), the discretized continuity equation in

DOI: 10.1002/fld

a matrix form is

$$\overline{w}_{i,j}^{n+1} = \overline{\overline{Bw}}\,\overline{u}_{i-1/2,j}^{n+1} + \overline{\overline{Cw}}\,\overline{u}_{i+1/2,j}^{n+1} + \overline{\overline{Dw}}\,\overline{v}_{i,j-1/2}^{n+1} + \overline{\overline{Ew}}\,\overline{v}_{i,j+1/2}^{n+1} \tag{8}$$

where the single overbar of u, v, and w represents a column vector and the double overbar of $\overline{\overline{Bw}}$, $\overline{\overline{Cw}}$, $\overline{\overline{Dw}}$, and $\overline{\overline{Ew}}$ denotes 2D matrices. The superscript index n in Equation (8) denotes time discretization.

Free-surface equation: The free-surface displacement is obtained by discretizing the free-surface equation (7) with the Crank–Nicolson scheme, i.e. yielding

$$\eta_{i,j}^{n+1} = \overline{Bfs}\,\overline{u}_{i-1/2,j}^{n+1} + \overline{Cfs}\,\overline{u}_{i+1/2,j}^{n+1} + \overline{Dfs}\,\overline{v}_{i,j-1/2}^{n+1} + \overline{Efs}\,\overline{v}_{i,j+1/2}^{n+1} + Ffs \tag{9}$$

where $\overline{Bfs}$, $\overline{Cfs}$, $\overline{Dfs}$, and $\overline{Efs}$ are constant column vectors.

Horizontal momentum equations: The Crank–Nicolson scheme is applied to discretize the horizontal momentum equations (2) and (3) in the x- and y-directions, respectively. The discretized horizontal momentum equations at positions $(i+\frac{1}{2}, j, k)$ and $(i, j+\frac{1}{2}, k)$ are

$$\overline{\overline{Ex_1}}\,\overline{u}_{i-1/2,j}^{n+1} + \overline{\overline{Ex_2}}\,\overline{u}_{i+1/2,j}^{n+1} + \overline{\overline{Ex_3}}\,\overline{u}_{i+3/2,j}^{n+1} + \overline{\overline{Fx_1}}\,\overline{P}_{i,j}^{n+1} + \overline{\overline{Fx_2}}\,\overline{P}_{i+1,j}^{n+1} = \overline{Gx_0} \tag{10a}$$

$$\overline{\overline{Ey_1}}\,\overline{v}_{i,j-1/2}^{n+1} + \overline{\overline{Ey_2}}\,\overline{v}_{i,j+1/2}^{n+1} + \overline{\overline{Ey_3}}\,\overline{v}_{i,j+3/2}^{n+1} + \overline{\overline{Fy_1}}\,\overline{P}_{i,j}^{n+1} + \overline{\overline{Fy_2}}\,\overline{P}_{i,j+1}^{n+1} = \overline{Gy_0} \tag{10b}$$

where $\overline{\overline{Ex_l}}$, $\overline{\overline{Ey_l}}$, $\overline{\overline{Fx_l}}$, and $\overline{\overline{Fy_l}}$, with $l=1, 2$, and 3, are all matrices. Note that for top-layer cells, the size of the cells varies with respect to the horizontal position and time. To calculate the horizontal pressure gradient, we interpolate the pressure $P_{i,j,N_3=3}$ to the same z level, $P'_{i,j,N_3=3}$ (see the open circle in Figure 1(b)). The similar procedure for the horizontal pressure gradient is applied to bottom-layer cells (see the open circle in Figure 1(d)) .

Vertical momentum equation: For layers below the top layer (Figure 1(c)), the Crank–Nicolson scheme is also applied to discretize the vertical momentum equation (4) at the position $(i, j, k+\frac{1}{2})$. Substituting Equation (8) of the vertical velocity into the discretized vertical momentum equation gives

$$P_{i,j,k}^{n+1} = P_{i,j,k+1}^{n+1} + \overline{Bvm}\,\overline{u}_{i-1/2,j}^{n+1} + \overline{Cvm}\,\overline{u}_{i+1/2,j}^{n+1} + \overline{Dvm}\,\overline{v}_{i,j-1/2}^{n+1} + \overline{Evm}\,\overline{v}_{i,j+1/2}^{n+1} + Fvm \tag{11}$$

where $\overline{Bvm}$, $\overline{Cvm}$, $\overline{Dvm}$, and $\overline{Evm}$ are constant column vectors. In Equation (11) the pressure at lower layers is related to the one at upper layers and its adjacent horizontal velocities. To explicitly express the pressure at lower layers, a top-layer pressure is needed. Instead of using the integration approach proposed by Yuan and Wu [44], in this paper we introduce analytical-based Boussinesq-type like equations to exactly describe the vertical pressure distribution. Details are presented next.

3.2. Embedded Boussinesq-type like equations

The existing NHM [44] is under a Cartesian staggered system. Here, we embed the Boussinesq-type like equations with a reference velocity [5] at a specific depth to optimize the linear wave dispersion property. Figure 2 shows the location of the reference velocity under a virtual grid system (dashed frames) and a non-hydrostatic physical grid system (solid frames). The reference location is specified by $z_B(x, y) = -\alpha_B \cdot h(x, y)$ where α_B is a parameter bounded between 0 and 1. There are three main steps.

DOI: 10.1002/fld

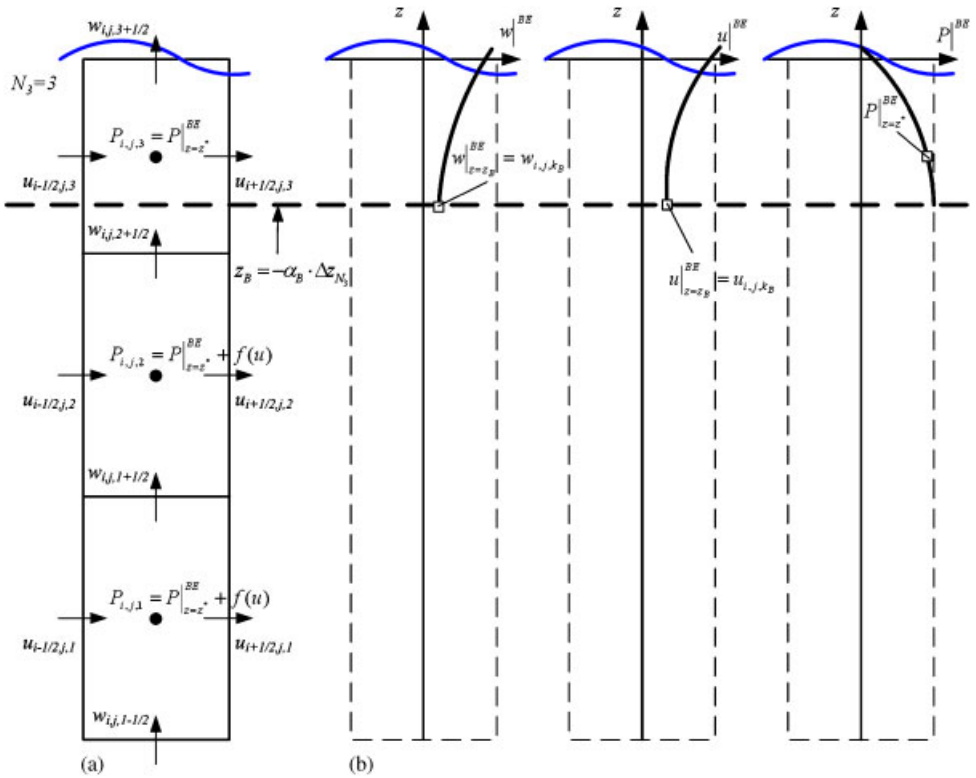

Figure 2. (a) Computational grids (solid frames) for the non-hydrostatic model and (b) virtual grids and the location of the reference velocity (dashed frames) for vertical velocity w, horizontal velocity u, and pressure P.

First, using Taylor expansion of the velocity at the reference location z_{B} we obtain the horizontal velocity profiles

$$u|^{\mathrm{BE}} \approx u|^{\mathrm{BE}}_{z=z_{\mathrm{B}}} + (z-z_{\mathrm{B}})\cdot \left.\frac{\partial u}{\partial z}\right|^{\mathrm{BE}}_{z=z_{\mathrm{B}}} + \frac{1}{2}\cdot(z-z_{\mathrm{B}})^2\cdot \left.\frac{\partial^2 u}{\partial z^2}\right|^{\mathrm{BE}}_{z=z_{\mathrm{B}}} \tag{12a}$$

$$v|^{\mathrm{BE}} \approx v|^{\mathrm{BE}}_{z=z_{\mathrm{B}}} + (z-z_{\mathrm{B}})\cdot \left.\frac{\partial v}{\partial z}\right|^{\mathrm{BE}}_{z=z_{\mathrm{B}}} + \frac{1}{2}\cdot(z-z_{\mathrm{B}})^2\cdot \left.\frac{\partial^2 v}{\partial z^2}\right|^{\mathrm{BE}}_{z=z_{\mathrm{B}}} \tag{12b}$$

where

$$u|^{\mathrm{BE}}_{z=z_{\mathrm{B}}},\quad v|^{\mathrm{BE}}_{z=z_{\mathrm{B}}},\quad \left.\frac{\partial u}{\partial z}\right|^{\mathrm{BE}}_{z=z_{\mathrm{B}}},\quad \left.\frac{\partial v}{\partial z}\right|^{\mathrm{BE}}_{z=z_{\mathrm{B}}}$$

$$\left.\frac{\partial^2 u}{\partial z^2}\right|^{\mathrm{BE}}_{z=z_{\mathrm{B}}} \quad \text{and} \quad \left.\frac{\partial^2 v}{\partial z^2}\right|^{\mathrm{BE}}_{z=z_{\mathrm{B}}}$$

DOI: 10.1002/fld

are calculated by imposing the continuous condition between the Boussinesq-type like equations and the NHM. In other words, $u|^{\mathrm{BE}}_{z=z_{\mathrm{B}}}=u_{i,j,k_{\mathrm{B}}}$ and $v|^{\mathrm{BE}}_{z=z_{\mathrm{B}}}=v_{i,j,k_{\mathrm{B}}}$, where $u_{i,j,k_{\mathrm{B}}}$, $v_{i,j,k_{\mathrm{B}}}$ are the reference velocities and can be obtained by the interpolation of the NHM, i.e. $u_{i,j,k_{\mathrm{B}}}=f_u(u_{i,j,k},u_{i,j,k\pm1})$ and $v_{i,j,k_{\mathrm{B}}}=f_v(v_{i,j,k},v_{i,j,k\pm1})$. The similar procedure is also performed to the rest of the first and second derivatives of horizontal velocities. Different from the Boussinesq-type equations [5, 6, 48], our embedded Boussinesq-type like equations are free of the irrotational flow assumption.

To determine the vertical velocity profile, we substitute Equations (12a) and (12b) into the integrated continuity equation (1) from the reference location z_{B} to an arbitrary location z, yielding

$$w|^{\mathrm{BE}}\approx w|^{\mathrm{BE}}_{z=z_{\mathrm{B}}}+(z-z_{\mathrm{B}})\cdot\left(-\frac{\partial u}{\partial x}-\frac{\partial v}{\partial y}\right)\Bigg|^{\mathrm{BE}}_{z=z_{\mathrm{B}}}+\frac{1}{2}\cdot(z-z_{\mathrm{B}})^2\cdot\left(-\frac{\partial^2 u}{\partial x\partial z}-\frac{\partial^2 v}{\partial y\partial z}\right)\Bigg|^{\mathrm{BE}}_{z=z_{\mathrm{B}}} \tag{13}$$

where

$$w|^{\mathrm{BE}}_{z=z_{\mathrm{B}}},\quad \left(-\frac{\partial u}{\partial x}-\frac{\partial v}{\partial y}\right)\Bigg|^{\mathrm{BE}}_{z=z_{\mathrm{B}}}\quad\text{and}\quad \left(-\frac{\partial^2 u}{\partial x\partial z}-\frac{\partial^2 v}{\partial y\partial z}\right)\Bigg|^{\mathrm{BE}}_{z=z_{\mathrm{B}}}$$

are evaluated at the reference location z_{B}. Similarly, we impose the continuous condition between the Boussinesq-type like equation and the NHM.

The final step is to obtain an analytical-based pressure profile. Integrating the vertical momentum equation (4) from z to the free surface, applying the Leibniz's rule, and substituting free-surface kinematic boundary condition (6) and free-surface pressure condition we obtain the pressure field

$$P=g(\eta-z)+\frac{\partial}{\partial t}\int_z^\eta w\,\mathrm{d}z+\frac{\partial}{\partial x}\int_z^\eta uw\,\mathrm{d}z+\frac{\partial}{\partial y}\int_z^\eta vw\,\mathrm{d}z-w^2|_z \tag{14}$$

Instead of directly discretizing the above equation for the top-layer cell [44], we substitute the analytical-based velocity profile of Equations (12a), (12b), and (13) into Equation (14), yielding

$$\begin{aligned}P|^{\mathrm{BE}}=&(\eta-z)\cdot\left(g+\frac{\partial E}{\partial t}+A\cdot\frac{\partial E}{\partial x}+C\cdot\frac{\partial E}{\partial y}+E\cdot F\right)\\&+\frac{1}{2}(\eta^2-z^2)\cdot\left(\frac{\partial F}{\partial t}+A\cdot\frac{\partial F}{\partial x}+B\cdot\frac{\partial E}{\partial x}+C\cdot\frac{\partial F}{\partial y}+D\cdot\frac{\partial E}{\partial y}+F^2\right)\end{aligned} \tag{15}$$

where

$$A=u|^{\mathrm{BE}}_{z=z_{\mathrm{B}}}-z_{\mathrm{B}}\cdot\frac{\partial u}{\partial z}\Bigg|^{\mathrm{BE}}_{z=z_{\mathrm{B}}},\quad B=\frac{\partial u}{\partial z}\Bigg|^{\mathrm{BE}}_{z=z_{\mathrm{B}}}$$

$$C=v|^{\mathrm{BE}}_{z=z_{\mathrm{B}}}-z_{\mathrm{B}}\cdot\frac{\partial v}{\partial z}\Bigg|^{\mathrm{BE}}_{z=z_{\mathrm{B}}},\quad D=\frac{\partial v}{\partial z}\Bigg|^{\mathrm{BE}}_{z=z_{\mathrm{B}}}$$

$$E=w|^{\mathrm{BE}}_{z=z_{\mathrm{B}}}-z_{\mathrm{B}}\cdot\left(-\frac{\partial u}{\partial x}-\frac{\partial v}{\partial y}\right)\Bigg|^{\mathrm{BE}}_{z=z_{\mathrm{B}}}\quad\text{and}\quad F=\left(-\frac{\partial u}{\partial x}-\frac{\partial v}{\partial y}\right)\Bigg|^{\mathrm{BE}}_{z=z_{\mathrm{B}}}$$

The vertical pressure distribution based on the Boussinesq-type like equations enables the NHM to evaluate the top-layer pressure without any approximation, i.e. $P_{i,j,N_3}=P|^{\mathrm{BE}}_{z=z^*}$, where z^* represents

DOI: 10.1002/fld

the level at the center of the top-layer cell. Discretizing Equation (15) using the Crank–Nicolson scheme, we obtain the top-layer pressure

$$P_{i,j,N_3}^{n+1} \approx a_{\mathrm{TNP0}}\eta_{i,j}^{n+1} + a_{\mathrm{TNP1}}w_{i,j,k_\mathrm{B}}^{n+1} + a_{\mathrm{TNP2}}u_{i-1/2,j,k_\mathrm{B}}^{n+1} + a_{\mathrm{TNP3}}u_{i+1/2,j,k_\mathrm{B}}^{n+1} + a_{\mathrm{TNP4}}v_{i,j-1/2,k_\mathrm{B}}^{n+1} + a_{\mathrm{TNP5}}v_{i,j+1/2,k_\mathrm{B}}^{n+1} + a_{\mathrm{TNP6}} \tag{16}$$

where the coefficients are

$$a_{\mathrm{TNP0}} = \frac{1}{\theta_{\mathrm{CNS}}} \cdot \left(\theta_{\mathrm{hs}} \frac{g}{2}\right)$$

$$a_{\mathrm{TNP1}} = \frac{1}{\theta_{\mathrm{CNS}}} \cdot (\eta_{i,j}^n - z_{i,j,N}) \cdot \frac{1}{\Delta t}$$

$$a_{\mathrm{TNP2}} = -a_{\mathrm{TNP3}} = \frac{1}{\theta_{\mathrm{CNS}}} \cdot (\eta_{i,j}^n - z_{i,j,N}^n) \cdot \frac{1}{\Delta t} \cdot (-z_\mathrm{B}) \cdot (-1) \cdot \left(\frac{-1}{\Delta x}\right) + \frac{1}{\theta_{\mathrm{CNS}}} \cdot \frac{1}{2} ({\eta_{i,j}^n}^2 - {z_{i,j,N}^n}^2) \cdot \frac{1}{\Delta t} \cdot (-1) \cdot \left(\frac{-1}{\Delta x}\right)$$

$$a_{\mathrm{TNP4}} = -a_{\mathrm{TNP5}} = \frac{1}{\theta_{\mathrm{CNS}}} \cdot (\eta_{i,j}^n - z_{i,j,N}^n) \cdot \frac{1}{\Delta t} \cdot (-z_\mathrm{B}) \cdot (-1) \cdot \left(\frac{-1}{\Delta y}\right) + \frac{1}{\theta_{\mathrm{CNS}}} \cdot \frac{1}{2} ({\eta_{i,j}^n}^2 - z_{i,j,N^n}^2) \cdot \frac{1}{\Delta t} \cdot (-1) \cdot \left(\frac{-1}{\Delta y}\right)$$

$$\begin{aligned} a_{\mathrm{NHP6}} = & -\frac{(1-\theta_{\mathrm{CNS}})}{\theta_{\mathrm{CNS}}} \cdot P_{i,j,N}^n + \frac{(1-\theta_{\mathrm{hs}})}{\theta_{\mathrm{CNS}}} \cdot \frac{g}{2} \cdot \eta_{i,j}^n + \frac{1}{\theta_{\mathrm{CNS}}} \cdot \frac{g}{2} \cdot \Delta z_N \\ & + \frac{1}{\theta_{\mathrm{CNS}}} \cdot (\eta_{i,j}^n - z_{i,j,N}^n) \cdot \left[\frac{-1}{\Delta t} \cdot E_{i,j,k_\mathrm{B}}^n + Aa_{i,j,k_\mathrm{B}}^n \cdot \frac{\partial}{\partial x} \cdot (Ea_{i,j,k_\mathrm{B}}^n) \right. \\ & \left. + Ca_{i,j,k_\mathrm{B}}^n \cdot \frac{\partial}{\partial y} \cdot (Ea_{i,j,k_\mathrm{B}}^n) + Ea_{i,j,k_\mathrm{B}}^n \cdot Fa_{i,j,k_\mathrm{B}}^n \right] \\ & + \frac{1}{\theta_{\mathrm{CNS}}} \cdot \frac{1}{2} \cdot ({\eta_{i,j}^n}^2 - {z_{i,j,N}^n}^2) \cdot \left[\frac{-1}{\Delta t} \cdot Fa_{i,j,k_\mathrm{B}}^n + Aa_{i,j,k_\mathrm{B}}^n \cdot \frac{\partial}{\partial x} \cdot (Fa_{i,j,k_\mathrm{B}}^n) \right. \\ & + Ba_{i,j,k_\mathrm{B}}^n \cdot \frac{\partial}{\partial x} \cdot (Ea_{i,j,k_\mathrm{B}}^n) + Ca_{i,j,k_\mathrm{B}}^n \cdot \frac{\partial}{\partial y} \cdot (Fa_{i,j,k_\mathrm{B}}^n) + \cdot Da_{i,j,k_\mathrm{B}}^n \cdot \frac{\partial}{\partial y} \cdot (Ea_{i,j,k_\mathrm{B}}^n) \\ & \left. + \frac{1}{\theta_{\mathrm{CNS}}} \cdot \frac{1}{2} \cdot ({\eta_{i,j}^n}^2 - {z_{i,j,N}^n}^2) \cdot (F_{i,j,k_\mathrm{B}}^n)^2 \right] + a_{\mathrm{NHP0}} \cdot Ffs \end{aligned}$$

DOI: 10.1002/fld

with

$$Aa_{i,j,k_B} = u_{i,j,k_B} - z_B \cdot \left(\frac{\partial u}{\partial z}\right)_{i,j,k_B}, \quad Ba_{i,j,k_B} = \left(\frac{\partial u}{\partial z}\right)_{i,j,k_B}$$

$$Ca_{i,j,k_B} = v_{i,j,k_B} - z_B \cdot \left(\frac{\partial v}{\partial z}\right)_{i,j,k_B}, \quad Da_{i,j,k_B} = \left(\frac{\partial v}{\partial z}\right)_{i,j,k_B}$$

$$Ea_{i,j,k_B} = w_{i,j,k_B} - z_B \cdot \left(-\frac{\partial u}{\partial x} - \frac{\partial v}{\partial y}\right)_{i,j,k_B} \quad \text{and} \quad Fa_{i,j,k_B} = \left(-\frac{\partial u}{\partial x} - \frac{\partial v}{\partial y}\right)_{i,j,k_B}$$

Substituting Equations (8) and (9) into Equation (16) gives the top-layer pressure

$$P^{n+1}_{i,j,N_3} = \overline{Btp}\,\overline{u}^{n+1}_{i-1/2,j} + \overline{Ctp}\,\overline{u}^{n+1}_{i+1/2,j} + \overline{Dtp}\,\overline{v}^{n+1}_{i,j-1/2} + \overline{Etp}\,\overline{v}^{n+1}_{i,j+1/2} + Ftp \tag{17}$$

where $\overline{Btp}$, $\overline{Ctp}$, $\overline{Dtp}$, and $\overline{Etp}$ are constant column vectors.

3.3. Overall algorithm

In this study, we present a novel method to analytically specify the top-layer pressure that is based on Boussinesq-type like equations. The pressure would be embedded into the NHM by imposing the continuous conditions at a reference location, allowing one free parameter to optimize linear wave properties [5]. In other words, the pressure field in Equation (14) can be directly determined by the embedded Boussinesq-type like equations without any approximation. Substituting the new top-layer pressures of Equation (17) and pressure at lower layers of Equation (11) into the discretized horizontal momentum equations (10a) and (10b) gives the new resulting matrix system:

$$\overline{\overline{Exu_1}}\,\overline{u}^{n+1}_{i-1/2,j} + \overline{\overline{Exu_2}}\,\overline{u}^{n+1}_{i+1/2,j} + \overline{\overline{Exu_3}}\,\overline{u}^{n+1}_{i+3/2,j} + \overline{\overline{Exv_1}}\,\overline{v}^{n+1}_{i,j-1/2} + \overline{\overline{Exv_2}}\,\overline{v}^{n+1}_{i,j+1/2} = \overline{Gx_1} \tag{18a}$$

$$\overline{\overline{Eyv_1}}\,\overline{v}^{n+1}_{i,j-1/2} + \overline{\overline{Eyv_2}}\,\overline{v}^{n+1}_{i,j+1/2} + \overline{\overline{Eyv_3}}\,\overline{v}^{n+1}_{i,j+3/2} + \overline{\overline{Eyu_1}}\,\overline{u}^{n+1}_{i-1/2,j} + \overline{\overline{Eyu_2}}\,\overline{u}^{n+1}_{i+1/2,j} = \overline{Gy_1} \tag{18b}$$

where $\overline{\overline{Exu_p}}$, $\overline{\overline{Exv_q}}$, $\overline{\overline{Eyv_p}}$, and $\overline{\overline{Eyu_q}}$ with $p = 1, 2$, and 3 and $q = 1$ and 2 are all matrices. With the embedded Boussinesq-type like equations, the form of resulting matrix system is the same but the coefficients are different from those in [44]. A domain decomposition method [32] is used to decompose the original matrix system of Equations (18a) and (18b) into a series of vertical 2D problems that can be solved by a direct block tri-diagonal matrix solver [49]. Convergence of all vertical 2D problems would be the solution of horizontal velocity at the updated time step. Finally, the vertical velocity component, free-surface elevation, and pressure are updated by back-substituting the solved horizontal velocity component.

4. NUMERICAL EXPERIMENTS

To examine the accuracy and efficiency of the new NHM-BTE, four examples of free-surface waves are used in our numerical experiments here. For all these examples, viscosity can be negligible and is therefore set to zero. First, we model the 2D free sloshing wave in a fixed tank to examine the effects of frequency dispersion. Results including surface displacement, velocity profile, and wave

DOI: 10.1002/fld

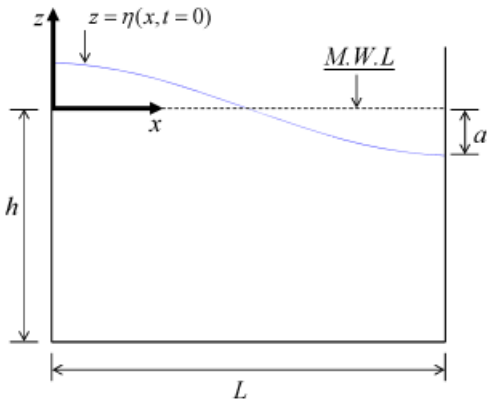

Figure 3. Configuration of an initial free-surface profile of a 2D free sloshing wave in a fixed tank.

celerity predicted by both NHM-BTE and NHM would be compared with analytical solutions. Next to examine the model's capability in predicting 3D surface displacement and velocity field, 3D forced sloshing wave with cross horizontal excitations is chosen. Results from both models will be compared with analytical solutions. Our last two examples are periodic wave propagation over a 2D submerged bar and a 3D elliptic shoal, which would be used to demonstrate the accuracy and efficiency of NHM-BTE in modeling nearshore wave transformation over uneven bottoms.

4.1. Free sloshing wave in a fixed tank

One of the common benchmark tests, free sloshing (standing) wave, is used to examine the accuracy and efficiency of NHM-BTE. Figure 3 shows the dimension of a 2D tank with a length L and still water depth $h=1$ m. Here, the first-mode free-surface sloshing wave, i.e. wave length $\lambda=2L$, is initially prescribed as

$$\eta(x,t=0)=a\cdot\cos(Kx)\cdot\cos(\omega t) \tag{19}$$

where a is the wave amplitude, $K=2\pi/\lambda$ is the wave number, and ω is the wave angular frequency and is determined by linear dispersion relation $\omega=\sqrt{gk\tanh(Kh)}$. Under linear wave theory, the horizontal velocity is

$$u(x,z,t)=\frac{agK}{\omega}\cdot\frac{\cosh[K(h+z)]}{\cosh(Kh)}\cdot\sin(Kx)\cdot\sin(\omega t) \tag{20}$$

To examine the effects of frequency dispersion, we use three different lengths of the sloshing tank ($L=4.0$, 2.0 and 1.0 m), giving $Kh=0.785$, 1.57, and 3.14, respectively, which are equivalent to nearly shallow-water, transitional-water, and deep-water conditions. The wave amplitude $a=0.01$ m is set to satisfy linear wave theory, yielding $aK=0.00785$, 0.0157, and $0.0314\ll1$ for the three tanks. In the model, the computational domain is discretized by 20 horizontal cells in the x direction and two and four vertical layers in the vertical z direction. For NHM, the size of each vertical layer is determined using the TDR technique [44] that maintains a fine resolution $K\Delta z$ from the top layers down to the one just above the bottom layer. For NHM-BTE, a TLC technique is proposed here. Specifically if $Kh\leqslant3.14$, a uniform vertical layer is applied. If $Kh>3.14$, the maximum

DOI: 10.1002/fld

Table I. Top-layer thickness and the reference velocity location for a two-layer NHM-BTE.

Kh	$K\Delta z_{\text{top}}$	$\Delta z_{\text{top}}/h$	$z_{\text{B}}/h=\alpha_{\text{B}}$
3.14	1.57	0.5	0.445
6	2.355	0.393	0.400
9	2.355	0.262	0.315
12	2.355	0.196	0.268
15	2.355	0.157	0.237

thickness of the top layer would be $K\Delta z_{top}=2.355$ ($75\%\times 3.14$) since the validity of Boussinesq-type equations is up to $kh=3.14$ [5, 48]. The rest of the layer(s) below are set to be uniform. After determining the layer thickness, we would set the reference velocity following Table I. Here, the reference location for these three tanks is $z_{\text{B}}(x, y)=-\alpha_{\text{B}}\cdot h(x, y)$, where $\alpha_{\text{B}}=0.445$ The time step is $\Delta t=Cr\cdot\Delta x/c$ by setting the Courant number $Cr=0.25$, where the wave phase speed

$$c_{\text{linear}}=\frac{\omega}{K}=\sqrt{\frac{g}{K}\tanh(Kh)}$$

Figures 4 and 5 show the comparison of the analytical solution and model results using two and four vertical layers, respectively. For the nearly shallow-water tank, the free-surface elevations at $x=0.025L$ calculated by the two-layer NHM and the two-layer NHM-BTE (Figure 4(a)) and the four-layer NHM and the four-layer NHM-BTE (Figure 5(a)) all match well with the analytical solution, demonstrating the capability of both NHM and NHM-BTE using small vertical layers in simulating shallow-water wave propagation. However, the free-surface elevation predicted by the two-layer NHM has a noticeable and significant lag in phase for the transitional-water tank (Figure 4(b)) and the deep-water tank (Figure 4(c)), respectively. The phase lag error in the transitional/deep tank can be corrected/decreased if the four-layer NHM is used (see Figure 5(b)/5(c)), indicating the importance of required vertical layer number in NHM for resolving wave frequency dispersion. In contrast to NHM, Figures 4(b) and 4(c) show that the two-layer NHM-BTE has well predicted the linear wave speed for the transitional-water tank and deep-water tank, demonstrating the significant role of our new top-layer pressure treatment in NHM-BTE in this paper. As a consequence further phase improvement by the four-layer NHM-BTE is not needed (Figures 5(b) and 5(c)).

To address the model's capability in resolving the velocity field, we use the deep-water dispersive tank here. Figure 6 shows the comparison between the predicted horizontal velocity profile and analytical solution at three stages, i.e. $t=5.25T$, $5.50T$, and $5.75T$. The horizontal velocity predicted by either the two- or four-layer NHM does not match with the analytical solution, supporting the phase lag errors found in the free-surface elevation in Figures 4(c) and 5(c). On the other hand, the two-layer NHM-BTE accurately resolves the velocity profile and wave phase speed, indicating that the new pressure field obtained from our embedded Boussinesq-type like equations plays an essential role in capturing linear dispersive wave propagation. From the viewpoint of efficiency, the two-layer NHM-BTE has achieved similar results obtained from the four-layer NHM-BTE. Compared with many other traditional NHMs [19–21, 24–27, 29, 30, 39] and efficient NHMs [32, 44–46] that require relatively a large number of vertical layers (5–20 cells) to satisfactorily simulate dispersive waves, the present approach that incorporates the Boussinesq-type like equations into the NHM is critical to further reduce required vertical layers.

DOI: 10.1002/fld

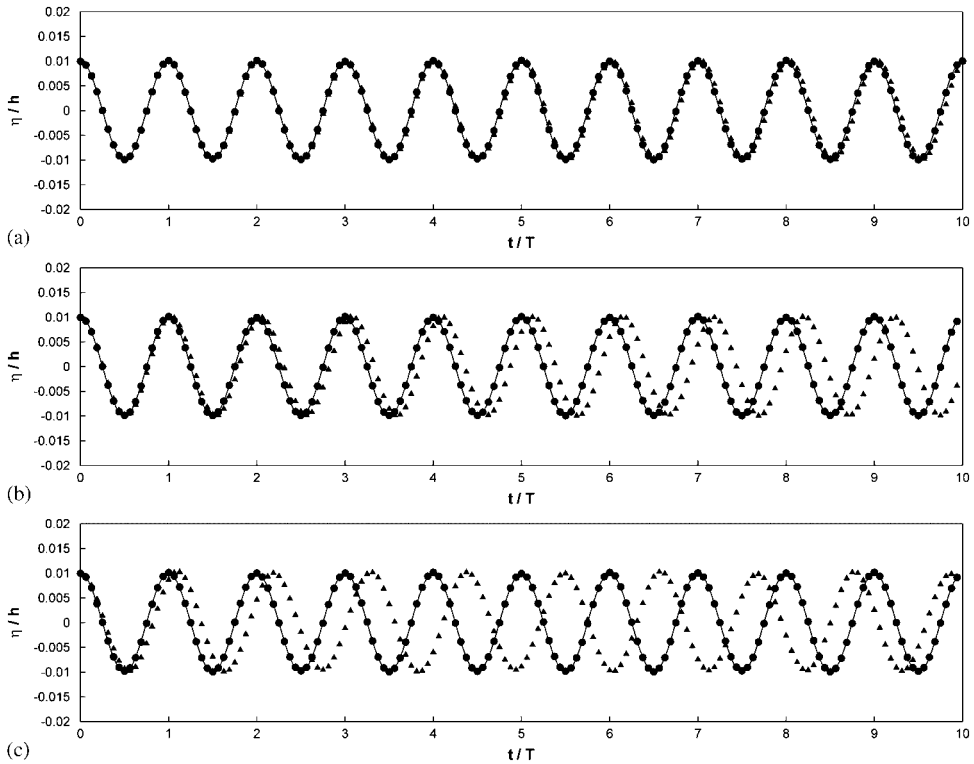

Figure 4. Computed free-surface elevation at $x = 0.025L$ of the three tanks: (a) $Kh = 0.785$; (b) $Kh = 1.57$; and (c) $Kh = 3.14$. Analytical solution (solid lines), two-layer NHM (solid triangles), and two-layer NHM-BTE (solid circles).

To quantify the above results predicted by the models, we use a relative error of wave speed, i.e. $\varepsilon_c = (c_{\text{model}} - c_{\text{linear}})/c_{\text{linear}}$ with c_{model} the phase speed predicted by the model. Figure 7 shows the normalized wave speed and relative error versus a non-dimensional relative water depth Kh. Note that for this numerical test we keep the water depth the same but vary the horizontal size of the tank. For NHM, the size of each vertical layer is determined using the TDR technique [44]. For NHM-BTE, the TLC technique is employed here to determine the optimal layer thickness (see Table I). Three main points are discussed here. First two- and four-layer NHMs both under-predict the wave speed. The error increases as Kh (the degree of dispersion) increases. Given an error tolerance $\varepsilon_c \leqslant 0.01$, two-layer NHM model is accurate up to $Kh = 1$ and four-layer NHM resolves linear dispersion up to $Kh \approx 3$. Interestingly, the error analysis supports the reported vertical layers (e.g. 2–4 cells) found in many wave propagation examples by Stelling and Zijlema [22], Yuan and Wu [32, 44], and Zijlema and Stelling [29]. Second, it is apparent that two-layer NHM-BTE has well resolved the wave phase speed up to $Kh \approx 12$, indicating the importance of the Boussinseq type like equations at the top-layer pressure treatment in deep-water wave modeling. Third four-layer NHM-BTE also resolves the wave phase speed of $Kh \approx 15$, and increasing the vertical layers would further facilitate wave modeling from offshore to nearshore. Overall the predicted results with error analysis of the free-sloshing wave example here not only exhibits the accuracy and efficiency of the

DOI: 10.1002/fld

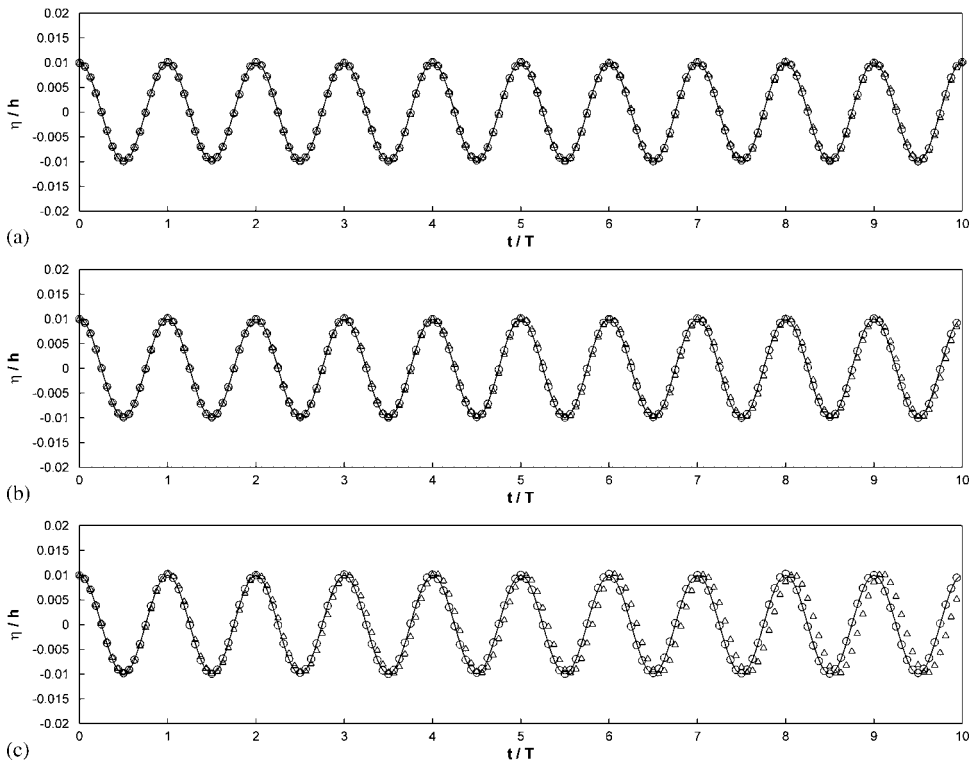

Figure 5. Same as Figure 4 except for four-layer NHM (open triangles) and four-layer NHM-BTE (open circles).

present model in modeling linear wave dispersion but also demonstrates the success of embedding the Boussinesq-type like equations with the TLC technique into the non-hydrostatic model.

4.2. Forced sloshing wave in a horizontal excited 3D tank

To examine the model's capability in predicting 3D surface wave displacement and velocity field, we apply the models to predict forced sloshing wave in a near-excited tank. Figure 8 shows the dimension of a 3D tank with $L_x = 1\,\mathrm{m}$ and $L_y = 1\,\mathrm{m}$ and the water depth $h = 1\,\mathrm{m}$, giving the natural frequency $\omega_{pq} = \sqrt{gK_{pq}\tanh(K_{pq}h)}$ with the corresponding wave mode (p, q) and wave number $K_{pq} = \sqrt{(p\pi/L_x)^2 + (q\pi/L_y)^2}$, where p and q are integers. To create a near-resonance sloshing condition, the tank is applied by cross horizontal accelerations $\ddot{x}(t) = -a_x \cdot \omega_x^2 \cdot \sin(\omega_x t)$ and $\ddot{y}(t) = -a_y \cdot \omega_y^2 \cdot \sin(\omega_y t)$, where a pair of overdots of $\ddot{x}(t)$ and $\ddot{y}(t)$ represents the second derivatives of displacement with respect to time; a_x and a_y, the magnitude of amplitude, are both equal to $0.372 \times 10^{-3}\,\mathrm{m}$; and ω_x and ω_y, the sloshing frequencies, are set to the first mode of near-resonant condition, i.e. $\omega_x = 0.9999\omega_{10}$ and $\omega_y = 0.9999\omega_{01}$, respectively.

While forced sloshing wave in a 2D/3D rectangular tank has been extensively studied [50–56], analytical solution for this condition here is rare. Following the approach for a 2D forced sloshing tank by Faltinsen *et al.* [51], we obtain the analytical solution by a superposition of Faltinsen's

DOI: 10.1002/fld

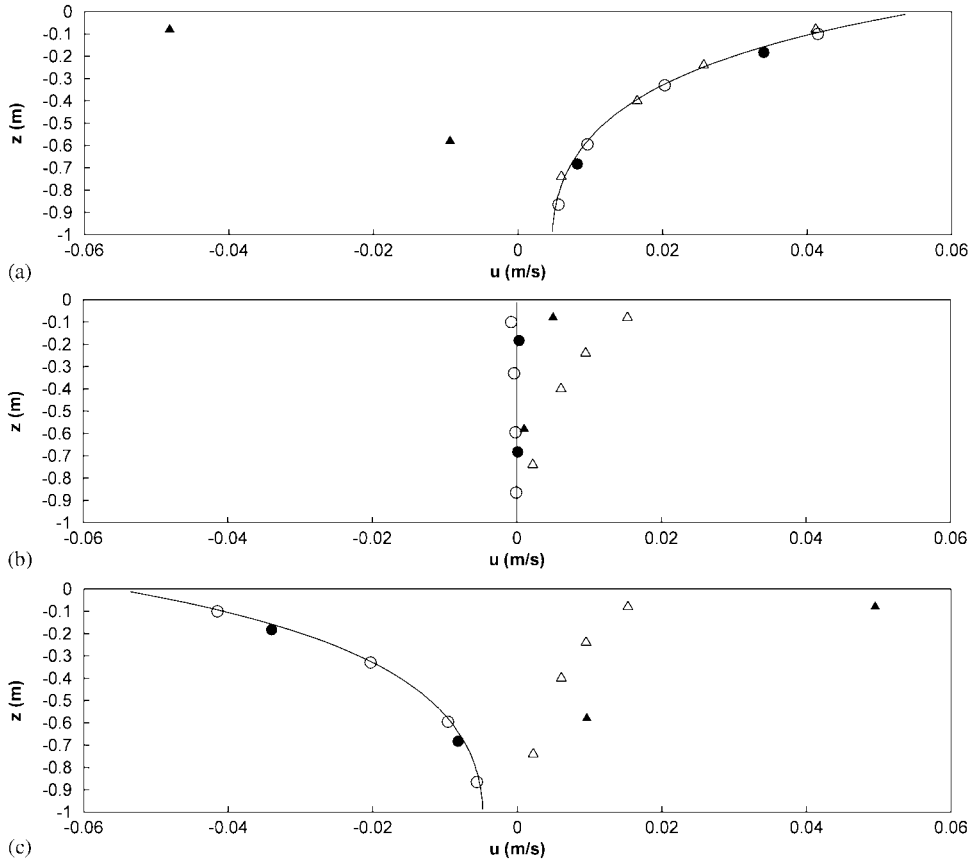

Figure 6. Computed horizontal velocity profiles in a deep-water tank ($Kh=3.14$) at $t=$(a) $5.25T$, (b) $5.50T$, and (c) $5.75T$. Analytical solution (solid lines), two-layer NHM (solid triangles), four-layer NHM (open triangles), two-layer NHM-BTE (solid circles), and four-layer NHM-BTE (open circles).

results in the x–z and y–z planes, yielding the surface displacement

$$\begin{aligned}\eta &= \eta_x + \eta_y \\ &= +\frac{a_x}{g}\cdot\left\{\left(x-\frac{L_x}{2}\right)\cdot\omega_x^2+\sum_{m=0}^{\infty}C_{m0}\cdot\omega_x\cdot\sin\left[K_{m0}\left(x-\frac{L_x}{2}\right)\right]\right\}\cdot\sin(\omega_x t) \\ &\quad -\frac{a_x}{g}\cdot\sum_{m=0}^{\infty}\omega_{m0}\cdot\left(C_{m0}+\frac{H_{m0}}{\omega_x^2}\right)\cdot\sin\left[K_{m0}\left(x-\frac{L_x}{2}\right)\right]\cdot\sin(\omega_{m0}t) \\ &\quad +\frac{a_y}{g}\cdot\left\{\left(y-\frac{L_y}{2}\right)\cdot\omega_y^2+\sum_{m=0}^{\infty}C_{0m}\cdot\omega_y\cdot\sin\left[K_{0m}\left(y-\frac{L_y}{2}\right)\right]\right\}\cdot\sin(\omega_y t) \\ &\quad -\frac{a_y}{g}\cdot\sum_{n=0}^{\infty}\omega_{0m}\cdot\left(C_{0m}+\frac{H_{0m}}{\omega_y^2}\right)\cdot\sin\left[K_{0m}\left(y-\frac{L_y}{2}\right)\right]\cdot\sin(\omega_{0m}t)\end{aligned} \tag{21}$$

DOI: 10.1002/fld

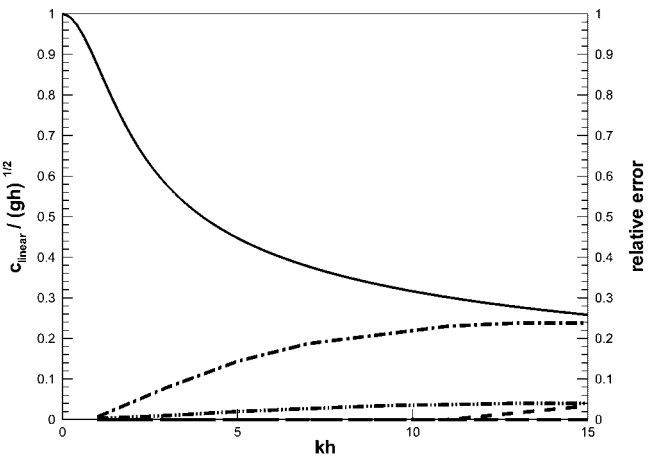

Figure 7. Normalized wave speed (solid lines) and relative error versus *Kh*. Two-layer NHM (▬ ▪ ▬), four-layer NHM (▬ ▪ ▪ ▬), two-layer NHM-BTE (short dashed line), and four-layer NHM-BTE (long dashed line).

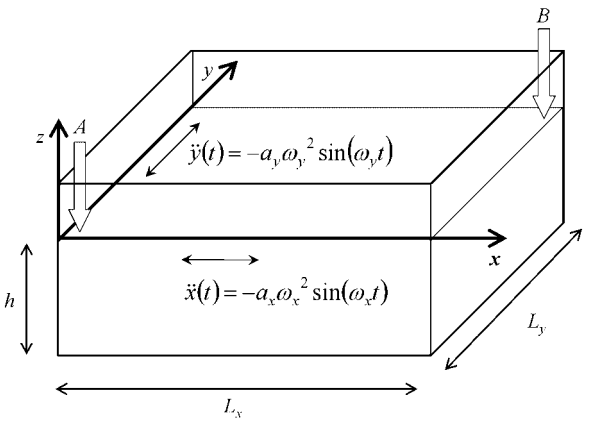

Figure 8. Configuration of a 3D forced sloshing wave in a moving tank. Two open arrows represent the locations A and B where time series of surface displacement are taken.

where

$$H_{m0} = \omega_x^3 \frac{4}{L_x} \frac{(-1)^m}{K_{m0}^2}, \quad H_{0m} = \omega_y^3 \frac{4}{L_y} \frac{(-1)^m}{K_{0m}^2}$$

$$C_{m0} = \frac{H_{m0}}{\omega_{m0}^2 - \omega_x^2} \quad \text{and} \quad C_{0m} = \frac{H_{0m}}{\omega_{0m}^2 - \omega_y^2}$$

DOI: 10.1002/fld

and the velocity fields

$$u = a_x \cdot \sum_{m=0}^{\infty} \left[C_{m0} \cdot \cos(\omega_x t) - \left(C_{m0} + \frac{H_{m0}}{\omega_x^2} \right) \cdot \cos(\omega_{m0} t) \right] \cdot \frac{\cosh[K_{m0}(z+h)]}{\cosh(K_{m0}h)} \times K_{m0} \cdot \cos\left[K_{m0} \left(x - \frac{L_x}{2} \right) \right] \tag{22a}$$

$$v = a_y \cdot \sum_{m=0}^{\infty} \left[C_{0m} \cdot \cos(\omega_y t) - \left(C_{0m} + \frac{H_{0m}}{\omega_y^2} \right) \cdot \cos(\omega_{0m} t) \right] \cdot \frac{\cosh[K_{0m}(z+h)]}{\cosh(K_{0m}h)} \times K_{0m} \cdot \cos\left[K_{0m} \left(y - \frac{L_y}{2} \right) \right] \tag{22b}$$

$$w = a_x \cdot \sum_{m=0}^{\infty} \left[C_{m0} \cdot \cos(\omega_x t) - \left(C_{m0} + \frac{H_{m0}}{\omega_x^2} \right) \cdot \cos(\omega_{m0} t) \right] \cdot \frac{\cosh[K_{m0}(z+h)]}{\cosh(K_{m0}h)} \times K_{m0} \cdot \sin\left[K_{m0} \left(x - \frac{L_x}{2} \right) \right] + a_y \cdot \sum_{n=0}^{\infty} \left[C_{0m} \cdot \cos(\omega_y t) - \left(C_{0m} + \frac{H_{0m}}{\omega_y^2} \right) \cdot \cos(\omega_{0m} t) \right] \times \frac{\cosh[K_{0m}(z+h)]}{\cosh(K_{0m}h)} \cdot K_{0m} \cdot \sin\left[K_{0m} \left(y - \frac{L_y}{2} \right) \right] \tag{22c}$$

In the model, a non-inertial moving frame with the cross horizontal acceleration motions is chosen to avoid the treatment of complicated boundary conditions at the moving walls. The resulting NSEs are the same except for the horizontal momentum equations:

$$\frac{\partial u}{\partial t} + u\frac{\partial u}{\partial x} + v\frac{\partial u}{\partial y} + w\frac{\partial u}{\partial z} = -\frac{\partial P}{\partial x} + \nu\frac{\partial^2 u}{\partial x^2} + \nu\frac{\partial^2 u}{\partial y^2} + \nu\frac{\partial^2 u}{\partial z^2} - \ddot{x}(t) \tag{23a}$$

$$\frac{\partial v}{\partial t} + u\frac{\partial v}{\partial x} + v\frac{\partial v}{\partial y} + w\frac{\partial v}{\partial z} = -\frac{\partial P}{\partial y} + \nu\frac{\partial^2 v}{\partial x^2} + \nu\frac{\partial^2 v}{\partial y^2} + \nu\frac{\partial^2 v}{\partial z^2} - \ddot{y}(t) \tag{23b}$$

The computational domain is discretized by a set of horizontally uniform 20×20 grids. For NHM, two and four vertical layers in the vertical z direction are employed following the TDR technique [44]. For NHM-BTE, only two vertical layers are used and the reference velocity is set following the TLC technique. The reference velocity is set at the bottom of the top-layer cell, i.e. $z_B(x, y) = -\alpha_B \cdot h(x, y)$, where $\alpha_B = 0.445$ The time step is determined by the Courant number $Cr = 0.25$ and the model runs up to $t = 10T$, where the wave period $T = 2\pi/\omega_{10} = 2\pi/\omega_{01} = 1.134$ s in this case. Initially ($t = 0$ s), the fluid is at rest. When $t > 0$ s, the sloshing motion subject to $x(t) = a_x \cdot \sin(\omega_x t)$ and $y(t) = a_y \cdot \sin(\omega_y t)$ is then applied.

Figure 9 shows the comparison of surface displacement time series at locations A ($x = 0.025L_x$, $y = 0.025L_y$) and B ($x = 0.975L_x$, $y = 0.975L_y$) between the analytical solution in Equation (21) and NHM and NHM-BTE. Consistent with our previous results of free sloshing wave, two-layer NHM (see Figure 9(a)) is incapable of predicting wave speed and amplitude

DOI: 10.1002/fld

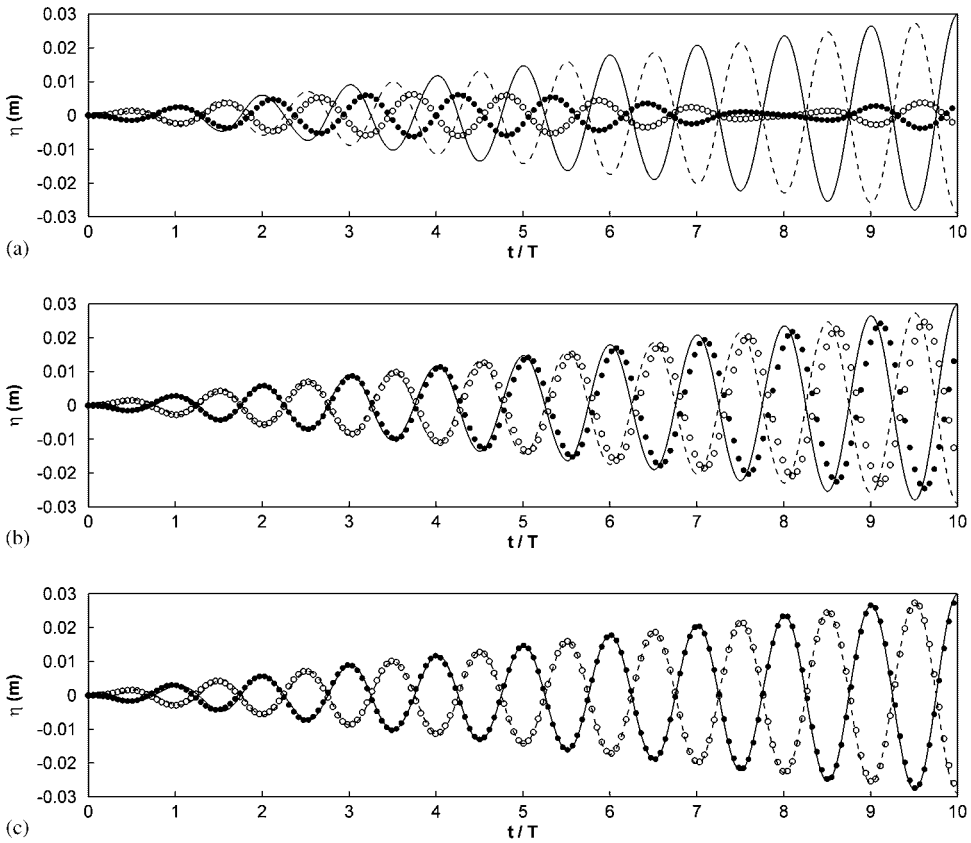

Figure 9. Computed surface displacement time series by (a) two-layer NHM, (b) four-layer NHM, and (c) two-layer NHM-BTE at location A—(solid circles) with analytical solution (solid lines) and location B—(open circles) with analytical solution (dashed lines).

under the $K_{10}h = K_{01}h = 3.14$ condition. Figure 9(b) shows that the four-layer NHM dramatically reduces the errors in phase speed and wave amplitude, further supporting the required vertical layer number results in Figure 7 if a NHM is used. In contrast, Figure 9(c) shows that the two-layer NHM-BTE has well-predicted phase speed and amplitude of forced sloshing waves, demonstrating the accuracy and efficiency of NHM-BTE in predicting 3D surface waves.

In Figure 10, the time series of the 3D velocity field time series by the analytical solution in Equation (22) and the two-layer NHM-BTE are depicted. It is of interest that horizontal velocities under forced sloshing waves are out of phase 180°, different from those in free sloshing waves. At $t = nT$ (where n is an integer), the velocity is zero everywhere and surface displacement reaches the maximum, yielding the maximum potential energy. Overall, the above results obtained by the two-layer NHM-BTE are in excellent agreement with analytical solutions. Compared with other NSE models by Wu *et al.* [52] with 12 vertical grids, Chen and Chiang [53, 55] with 20 vertical grids, and Kim [54] with 30 vertical grids, the NHM-BTE employing two vertical layers efficiently and accurately simulates 3D surface wave motions. Finally to the best of our knowledge, no

DOI: 10.1002/fld

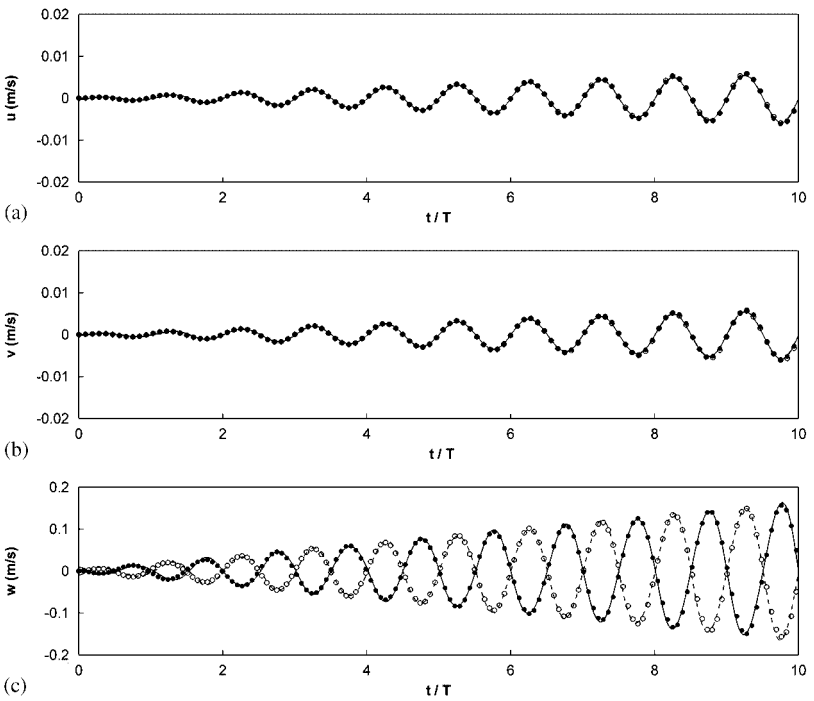

Figure 10. Comparison of velocity field: (a) u; (b) v; and (c) w time series between two-layer NHM-BTE (solid circles, open circles) and analytical solution (solid lines, dashed lines) at locations (A, B), respectively.

velocity field results under this condition obtained with a NHM and analytical solution have been published earlier.

4.3. Wave propagation over a 2D submerged bar

In this example we aim to examine NHM-BTE's capability in modeling wave deformation over uneven bottoms. In the past, a great deal of efforts has been paid to investigate wave interactions with irregular bathymetry (e.g. submerged bar) using physical experiments [57–59] or numerical simulations [19–23, 25, 27, 29, 31, 32, 44, 46, 48]. In this study, the experimental setup (see Figure 11) by Nakaoda *et al.* [58] is used. The wave flume has a length of 30 m with a still water depth $h_0 = 0.3$ m and $h_b = 0.1$ m at the submerged bar. The upward and downward slopes of the bar are 1:20 and 1:10, respectively. At the inflow boundary, an incident wave condition with wave height $H_0 = 2.0$ cm and wave period $T_0 = 1.5$ s is used here, yielding $K_0 h_0 = 0.80$. Free-surface elevations were measured at seven stations. In addition, the velocity fields were measured at the depth of $z = -0.02$ m, -0.16 m, and -0.26 m at station 7 to examine wave decomposition on the downward slope.

In the model, the computational domain is discretized by 1200 uniform grids along the x direction. For NHM, three non-uniform vertical layers ($\Delta z = 0.06$, 0.06, and 0.18 m) are used. For NHM-BTE, only two vertical layers ($\Delta z = 0.07$ and 0.23 m) are used and the reference velocity

DOI: 10.1002/fld

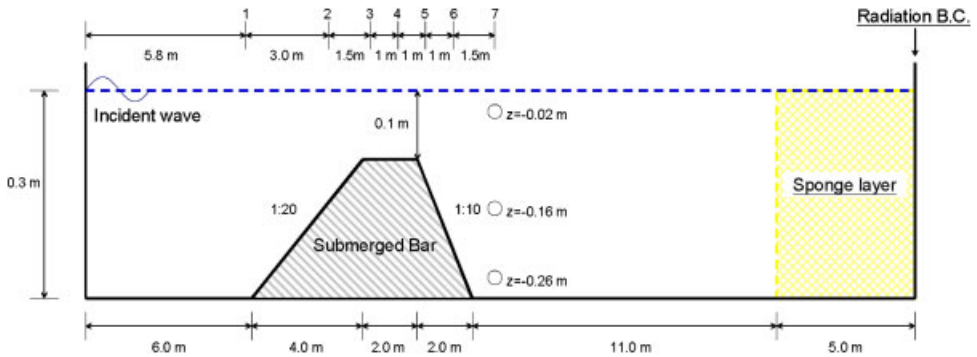

Figure 11. Sketch of the experimental setup and measurement stations by Nakaoda *et al.* [58]. Open circles represent the locations where velocity measurements were taken.

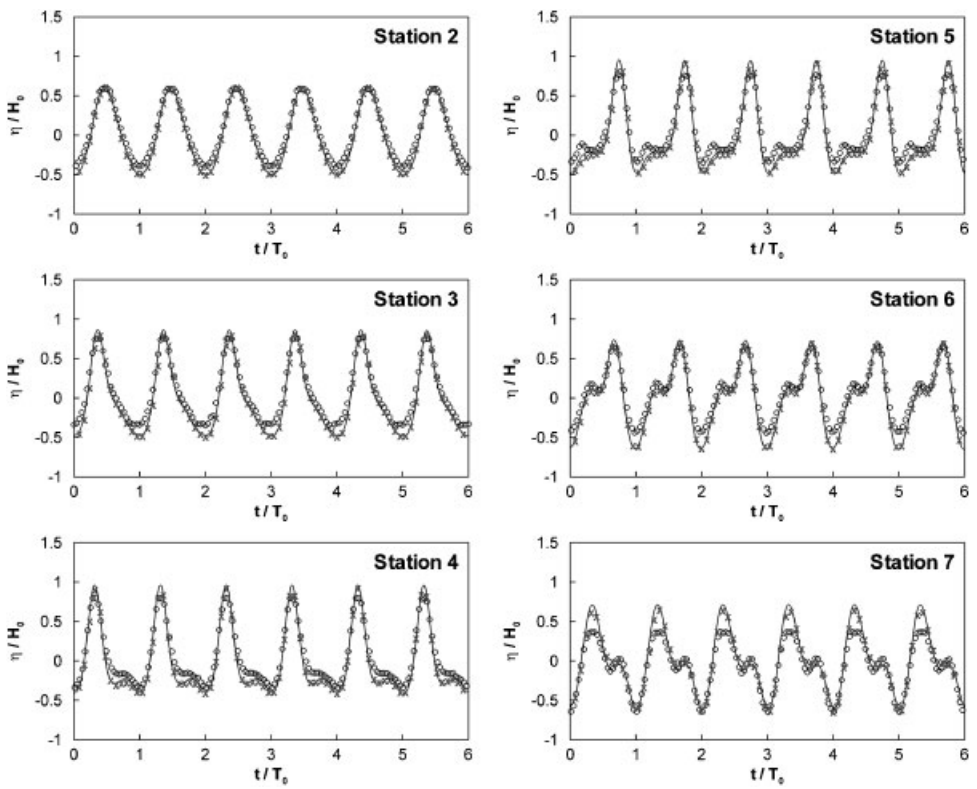

Figure 12. Comparison of the free-surface displacement at six measurement stations among experimental data (circles), three-layer NHM (x), and two-layer NHM-BTE (solid lines).

is set at $z_B(x, y) = -\alpha_B \cdot h(x, y)$, where $\alpha_B = 0.445$. At the outflow boundary, the Sommerfeld radiation boundary condition coupled with a sponge layer is used. Similar to the previous two examples, the time step determined by $Cr = 0.25$ is used.

DOI: 10.1002/fld

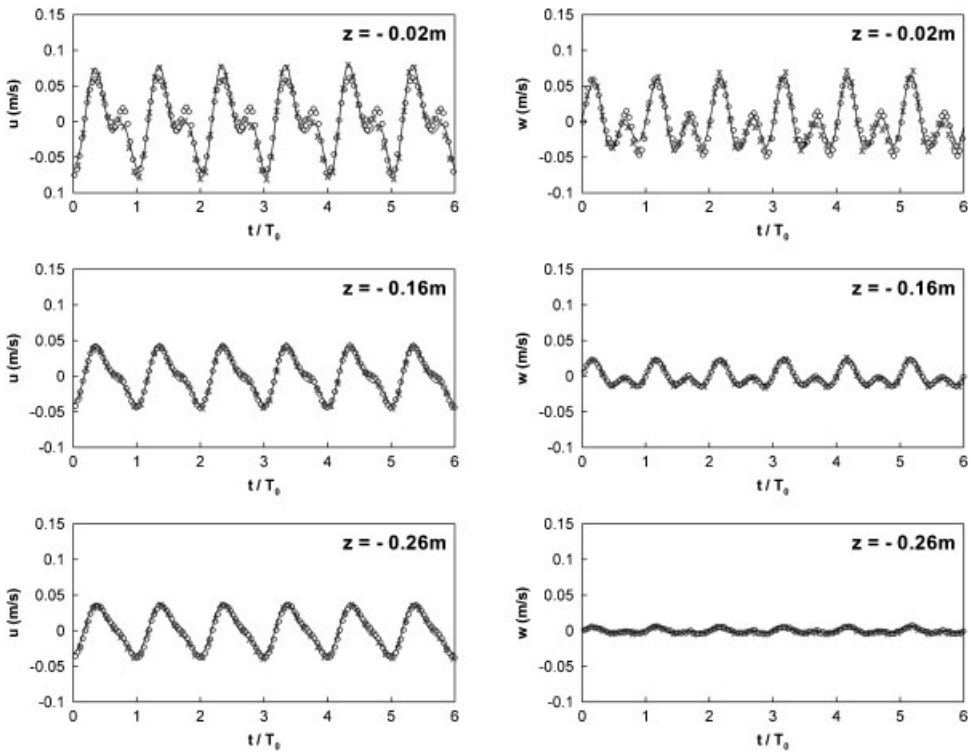

Figure 13. Comparison of horizontal u and vertical w velocities at station 7 among experimental data (circles), three-layer NHM (x), and two-layer NHM-BTE (solid lines).

Figure 12 compares the free-surface elevations between model results and laboratory measurements at six stations (from station 2 to station 7). As the incident wave propagates onto the upward slope at stations 2 and 3, shoaling occurs and wave becomes steeper. As the wave rides on the top of the bar, the development of higher harmonic due to nonlinearity occurs at stations 4 and 5. After that the release of generated higher harmonic appears on the lee side of the submerged bar at stations 6 and 7. Consistent with NHMs [23, 44], slight discrepancies in the peak surface displacement predicted by NHE-BTE appear at station 7, which may be due to the turbulence generated by the lee side of the submerged bar [21, 37] or measurement issues [58]. However, the overall results of surface displacement or wave height predicted by the two-layer NHM-BTE and the three-layer NHM are in a good agreement with experimental data, demonstrating the NHM-BTE's capability in predicting dispersive and nonlinear wave characteristics over uneven bottoms.

Figure 13 shows the excellent comparison of velocity fields between model results and experimental measurements at the three different depths at station 7. The two-layer NHM-BTE clearly captures the phenomena of wave decomposition in both horizontal and vertical velocity components. Overall the above results indicate that NHM-BTE developed in this paper has the advantages of efficiency and accuracy over traditional non-hydrostatic models in terms of required vertical layers [19–21, 25, 27, 46]. In addition, NHM-BTE has the capabilities in resolving velocity profiles, which cannot be easily obtained by traditional Boussinesq equations.

DOI: 10.1002/fld

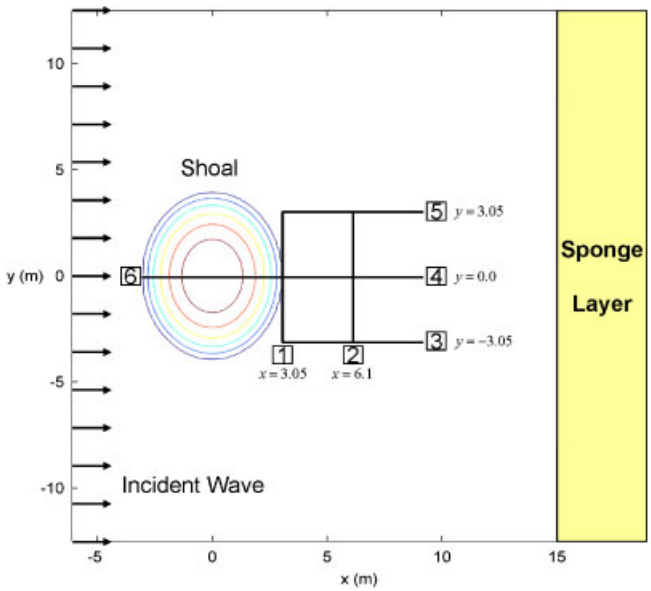

Figure 14. Sketch of the experimental setup, waves over an elliptic shoal and measurement sections, by Vincent and Briggs [60].

4.4. Wave propagation over a 3D elliptic shoal

Our last example is to model wave transformation over 3D varying bathymetries. In this study we use non-breaking monochromatic wave experiments over an elliptic shoal by Vincent and Briggs [60]. Figure 14 shows the experimental setup that consists of an elliptic shoal resting on a flat bottom with a constant water depth $h_0 = 0.4572\,\text{m}$ outside the shoal. The boundary of the elliptic shoal is

$$\left(\frac{x}{3.05}\right)^2 + \left(\frac{y}{3.96}\right)^2 = 1 \tag{24}$$

and the water depth inside the shoal area is

$$h_s = 0.9144 - 0.762\sqrt{1 - \left(\frac{x}{3.81}\right)^2 + \left(\frac{y}{4.95}\right)^2} \tag{25}$$

Wave heights were measured along the six cross sections.

In the model, the computational domain covers $25\,\text{m} \times 25\,\text{m}$ ($x = -6.1$ to $18.9\,\text{m} \times y = -12.5$ to $12.5\,\text{m}$). At the inflow boundary, an incident progressive wave with a wave height $H_0 = 2.54\,\text{cm}$ and period $T_0 = 1.3\,\text{s}$ is specified, yielding $K_0 h_0 = 1.27$. At the outflow boundary, a combination of a radiation boundary condition and a sponge layer technique is used. At the two lateral boundaries, impermeable and free-slip boundary conditions are applied. In other words, the velocity component normal to the wall is zero and the normal gradient for the tangential velocity components is also zero. The computational domain is discretized by a set of 500×250 horizontal grids. According to the required layer in Figure 7, two vertical layers are employed and the thickness of the top-layer cell is 0.08 m. The reference velocity is at $z_B(x, y) = -\alpha_B \cdot h(x, y)$, where $\alpha_B = 0.445$. The time

DOI: 10.1002/fld

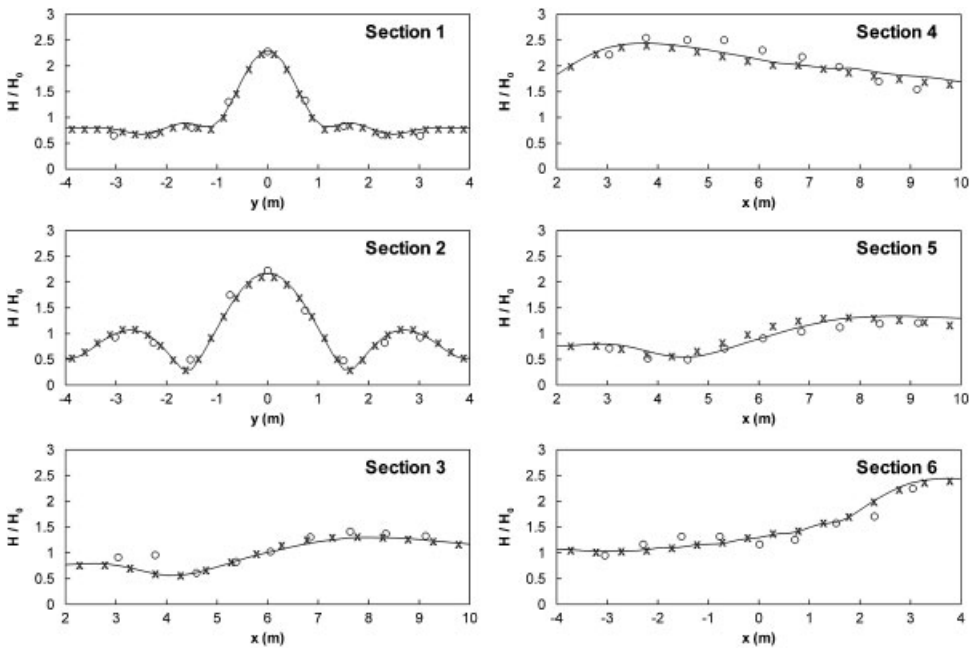

Figure 15. Comparison of normalized wave height H/H_0 among experimental data (circles), two-layer NHM (x), and two-layer NHM-BTE (solid lines).

step is taken as 0.02 s and the total simulation time is 34 s to achieve a stationary wave condition. The representative wave height H is obtained by averaging over the last four wave periods.

Figure 15 shows the comparison of model results and measurements of the relative wave height H/H_0 at the six cross sections. Along section 6, the wave propagates over the elliptic shoal and the wave becomes steeper due to the shoaling effect. Behind the elliptic shoal, refraction takes place, leading the focusing location at the center of section 1 and reaches the maximum relative wave height $H/H_0 = 2.5$ at $x = 4$ m along section 4. After wave focusing, diffraction occurs and wave energy spreads laterally, which is clearly seen along section 2. The energy spreading leads to wave re-focusing after $x = 5$ m along the sections 3 and 5. Figure 16 shows a perspective view of the fully developed 3D wave passing over an elliptic shoal. Overall the results predicted by both two-layer NHE-BTE and two-layer NHE are in excellent agreements with the measurements. Specifically the two-layer NHE-BTE gives slightly better results, further demonstrating the success of incorporating of Boussinesq-type like equations within the 3D NHM framework. Compared with other NSE models by Li and Fleming [20] using 11 vertical grids, NHE-BTE using only two vertical layers has accurately predicted 3D wave transformation including shoaling, refraction, diffraction, and focusing processes.

5. CONCLUSIONS

In this paper, a novel approach that embeds the Boussinesq-type like equations into the NHM at the top-layer pressure is developed. Instead of using an integration method [44], we introduce

DOI: 10.1002/fld

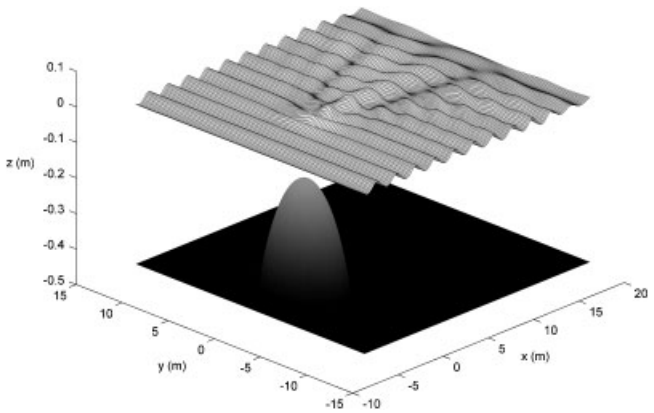

Figure 16. A perspective view for periodic wave propagation over an elliptic shoal.

the Boussinesq-type like equations under a virtual grid system into the NHM [32]. The top-layer pressure is therefore analytically expressed with no assumptions of irrotational and inviscid flow. The TCL technique is proposed and a reference location is used to optimize linear wave dispersion property.

The efficiency and accuracy of the newly developed NHM-BTE are examined through four examples. Results of the free sloshing wave example show that given an error tolerance of $\varepsilon_c \leqslant 0.01$ a two-layer NHM-BTE well resolves the wave phase speed up to $Kh \approx 12$, in comparison with $Kh = 1$ by a two-layer NHM and $Kh \approx 3$ by a four-layer NHM. A two-layer NHM-BTE also well predicts phase speed, wave amplitude, and velocity field of the forced sloshing wave, demonstrating NHM-BTE's capability in predicting free-surface wave using a very small amount of vertical layers. For wave propagation over a 2D submerged bar example, a two-layer NHM-BTE can accurately resolve the phenomena of wave decomposition in surface displacement. In addition, NHM-BTE has the capabilities in resolving velocity profiles, which cannot be easily obtained by the traditional Boussinesq equations. Finally, a two-layer NHM-BTE is shown to accurately predict wave transformation over a 3D varying shoal including shoaling, refraction, diffraction, and focusing processes. Overall this type of models, i.e. NHM-BTE models using two vertical layers, in contrast to models based on the Boussinesq-type equations [3, 5, 17, 48], would allow us to effectively and accurately simulate large-scale (10 km $\times$ 10 km) wave propagation from offshore deep water to nearshore shallow water. Progress on this application will be reported later.

ACKNOWLEDGEMENTS

The research is partly supported by the National Science Council of the Republic of China, Taiwan, under the Grant number 096-2917-I-002-036 for the first author, and the NSF-OCE-0628560—The carbon balance of Lake Superior: modeling lake processes and understanding impacts of regional carbon cycle, and the NSF North Temperate Lakes LTER program. The authors specifically thank Dr Jim Chen at Louisiana State University for his insightful experience and valuable suggestions on the characteristics and development of the Boussinesq equations.

DOI: 10.1002/fld

REFERENCES

1. Mei CC, Liu PLF. Surface waves and coastal dynamics. *Annual Review of Fluid Mechanics* 1993; **25**:215–240.
2. Liu PLF, Losada IJ. Wave propagation modeling in coastal engineering. *Journal of Hydraulic Research* 2002; **40**(3):229–240.
3. Peregrine DH. Long waves on a beach. *Journal of Fluid Mechanics* 1967; **27**:815–827.
4. Madsen PA, Murray R, Sørensen OR. A new form of the Boussinesq equations with improved linear dispersion characteristics. *Coastal Engineering* 1991; **15**(4):371–388.
5. Nwogu O. Alternative form of Boussinesq equations for nearshore wave propagation. *Journal of Waterway*, *Port*, *Coastal and Ocean Engineering* 1993; **119**:618–638.
6. Wei G, Kirby JT, Grilli ST, Subramanya R. A fully nonlinear Boussinesq model for surface waves. I. Highly nonlinear unsteady waves. *Journal of Fluid Mechanics* 1995; **294**:71–92.
7. Agnon Y, Madsen PA, Schäffer H. A new approach to high order Boussinesq models. *Journal of Fluid Mechanics* 1999; **399**:319–333.
8. Gobbi MF, Kirby JT, Wei G. A fully nonlinear Boussinesq model for surface waves. II. Extension to $O((kh)^4)$. *Journal of Fluid Mechanics* 2000; **405**:182–210.
9. Wu TY. A unified theory for modeling water waves. *Advances in Applied Mechanics* 2001; **37**:1–88.
10. Madsen PA, Bingham HB, Liu H. A new Boussinesq method for fully nonlinear waves from shallow to deep water. *Journal of Fluid Mechanics* 2002; **462**:1–30.
11. Dingemans M. *Water Wave Propagation over Uneven Bottoms*. Advanced Series on Ocean Engineering, vol. 13. World Scientific: Singapore, 1997.
12. Madsen PA, Schäffer HA. A review of Boussinesq-type equations for gravity waves. In *Advances in Coastal and Ocean Engineering*, vol. 5, Liu P (ed.). World Scientific: Singapore, 1–95.
13. Kirby JT. Boussinesq models and applications to nearshore wave propagation, surf zone processes and wave-induced currents. *Advances in Coastal Modeling* 2003; **67**:1–41.
14. Kennedy AB, Chen Q, Kirby JT, Dalrymple RA. Boussinesq modeling of wave transformation, breaking, end runup. I: 1D. *Journal of Waterway*, *Port*, *Coastal and Ocean Engineering* 2000; **126**(1):39–47.
15. Chen Q, Kirby JT, Dalrymple RA, Kennedy AB, Chawla A. Boussinesq modeling of wave transformation, breaking, and runup, II: 2D. *Journal of Waterway*, *Port*, *Coastal and Ocean Engineering* 2000; **126**:48–56.
16. Veeramony J, Svendsen IA. The flow in surf-zone waves. *Coastal Engineering* 2000; **39**(2–4):93–122.
17. Hsiao SC, Lynett P, Hwung HH, Liu PLF. Numerical simulations of nonlinear short waves using a multilayer model. *Journal of Engineering Mechanics* 2005; **131**(3):231–243.
18. Chorin AJ. Numerical solution of Navier–Stokes equations. *Mathematics of Computation* 1968; **22**:745–762.
19. Mayer S, Garapon A, Sorensen LS. A fractional step method for unsteady free-surface flow with applications to non-linear wave dynamics. *International Journal for Numerical Methods in Fluids* 1998; **28**:293–315.
20. Li B, Fleming CA. Three-dimensional model of Navier–Stokes equations for water waves. *Journal of Waterway*, *Port*, *Coastal and Ocean Engineering* 2001; **127**:16–25.
21. Lin P, Li CW. A σ-coordinate three-dimensional numerical model for surface wave propagation. *International Journal for Numerical Methods in Fluids* 2002; **38**:1045–1068.
22. Stelling G, Zijlema M. An accurate and efficient finite-difference algorithm for non-hydrostatic free-surface flow with application to wave propagation. *International Journal for Numerical Methods in Fluids* 2003; **43**(1):1–23.
23. Choi DY, Wu CH. A new efficient 3D non-hydrostatic free-surface flow model for simulating water wave motions. *Ocean Engineering* 2006; **33**(5–6):587–609.
24. Anthonio SL, Hall KR. High-order compact numerical schemes for non-hydrostatic free surface flows. *International Journal for Numerical Methods in Fluids* 2006; **52**:1315–1337.
25. Casulli V. A semi-implicit finite difference method for non-hydrostatic, free-surface flows. *International Journal for Numerical Methods in Fluids* 1999; **30**:425–440.
26. Kocyigit MB, Falconer RA, Lin B. Three-dimensional numerical modeling of free surface flows with non-hydrostatic pressure. *International Journal for Numerical Methods in Fluids* 2002; **40**(9):1145–1162.
27. Chen X. A fully hydrodynamic model for three-dimensional, free-surface flows. *International Journal for Numerical Methods in Fluids* 2003; **42**(9):929–952.
28. Zijlema M, Stelling G. Further experiences with computing non-hydrostatic free-surface flows involving water waves. *International Journal for Numerical Methods in Fluids* 2005; **48**:169–197.
29. Lee JW, Teubner MD, Nixon JB, Gill PM. A 3-D non-hydrostatic pressure model for small amplitude free surface flows. *International Journal for Numerical Methods in Fluids* 2006; **50**(6):649–672.

DOI: 10.1002/fld

30. Namin M, Lin B, Falconer R. An implicit numerical algorithm for solving non-hydrostatic free-surface flow problems. *International Journal for Numerical Methods in Fluids* 2001; **35**:341–356.
31. Yuan H, Wu CH. A two-dimensional vertical non-hydrostatic s model with an implicit method for free-surface flows. *International Journal for Numerical Methods in Fluids* 2004; **44**(8):811–835.
32. Yuan H, Wu CH. An implicit 3D fully non-hydrostatic model for free-surface flows. *International Journal for Numerical Methods in Fluids* 2004; **46**(7):709–733.
33. Young CC, Wu CH, Kuo JT, Liu WC. A higher-order σ-coordinate non-hydrostatic model for nonlinear surface waves. *Ocean Engineering* 2007; **34**(10):1357–1370.
34. Harlow FH, Welch JE. Numerical calculation of time-dependent viscous incompressible flow of fluid with free surface. *Physics of Fluids* 1965; **8**:2182–2189.
35. Park JC, Kim MH, Miyata H. Fully non-linear free-surface simulations by a 3D viscous numerical wave tank. *International Journal for Numerical Methods in Fluids* 1999; **29**(6):685–703.
36. Hirt CW, Nichols BD. Volume of fluid (VOF) method for the dynamic of free boundaries. *Journal of Computational Physics* 1981; **39**(1):201–225.
37. Lin PZ, Liu PLF. A numerical study of breaking waves in the surf zone. *Journal of Fluid Mechanics* 1998; **359**:239–264.
38. Hirt CW, Amsden AA, Cook JL. An arbitrary Lagrangian Eulerian computing methods for all flow speeds. *Journal of Computational Physics* 1974; **14**:227–253.
39. Zhou JG, Stansby PK. An arbitrary Lagrangian–Eulerian σ (ALES) model with non-hydrostatic pressure for shallow water flows. *Computer Methods in Applied Mechanics and Engineering* 1999; **178**:199–214.
40. Osher S, Fedkiw RP. Level set methods: an overview and some recent results. *Journal of Computational Physics* 2001; **169**(2):463–502.
41. Iafrati A, Di Mascio A, Campana EF. A level set technique applied to unsteady free surface flows. A domain decomposition approach to compute wave breaking (wave-breaking flows). *International Journal for Numerical Methods in Fluids* 2003; **41**(4):419–445.
42. Nichols BD, Hirt CW. Calculating three-dimensional free surface flows in the vicinity of submerged and exposed structures. *Journal of Computational Physics* 1974; **12**:227–246.
43. Huang CJ, Zhang EC, Lee JF. Numerical simulation of nonlinear viscous wavefields generated by piston wave makers. *Journal of Engineering Mechanics* 1998; **124**(10):1110–1120.
44. Yuan H, Wu CH. Fully nonhydrostatic modeling of surface waves. *Journal of Engineering Mechanics* 2006; **132**(4):447–456.
45. Ahmadi A, Badiei P, Namin M. An implicit two-dimensional non-hydrostatic model for free-surface flows. *International Journal for Numerical Methods in Fluids* 2007; **54**(9):1055–1074.
46. Bradford SF. Godunov-based model for nonhydrostatic wave dynamics. *Journal of Waterway, Port, Coastal and Ocean Engineering* 2005; **131**(5):226–238.
47. Pacanowski RC, Gnanadesikan A. Transient response in a z-level ocean model that resolves topography with partial cells. *Monthly Weather Review* 1998; **126**(12):3248–3270.
48. Lynett P, Liu PLF. A two-layer approach to wave modeling. *Proceedings of the Royal Society of London, Series A* 2004; **460**(2049):2637–2669.
49. Keller HB. Accurate difference methods for nonlinear two-point boundary value problems. *SIAM Journal on Numerical Analysis* 1974; **11**(2):305–320.
50. Abramson HN. The dynamic behaviour of liquids in moving containers. *Report SP 106 of NASA*, 1966.
51. Faltinsen OM. A nonlinear theory of sloshing in rectangular tanks. *Journal of Ship Research* 1974; **18**(4): 224–241.
52. Wu GX, Ma QW, Eatock Taylor R. Numerical simulation of sloshing waves in a 3D tank based on a finite element method. *Applied Ocean Research* 1998; **20**:337–355.
53. Chen BF, Chiang HW. Complete 2D and fully nonlinear analysis of ideal fluid in tanks. *Journal of Engineering Mechanics* 1999; **125**(1):70–78.
54. Kim Y. Numerical simulation of sloshing flows with impact loads. *Applied Ocean Research* 2001; **23**:53–62.
55. Chen BF, Nokes R. Time-independent finite difference analysis of fully non-linear and viscous fluid sloshing in a rectangular tank. *Journal of Computational Physics* 2005; **209**(1):53–87.
56. Faltinsen OM, Rognebakke OF, Timokha AN. Classification of three-dimensional nonlinear sloshing in a square-base tank with finite depth. *Journal of Fluids and Structures* 2005; **20**:81–103.
57. Beji S, Battjes JA. Experimental investigation of wave propagation over a bar. *Coastal Engineering* 1993; **19**:151–162.

DOI: 10.1002/fld

58. Nadaoka K, Beji S, Nakakawa Y. A fully-dispersive nonlinear wave model and its numerical solutions. *Proceedings of the 24th International Conference on Coastal Engineering ASCE*, Kobe, Japan, 1994; 427–441.
59. Ohyama T, Kiota W, Tada A. Applicability of numerical models to nonlinear dispersive waves. *Coastal Engineering* 1995; **24**:297–313.
60. Vincent CL, Briggs MJ. Refraction–diffraction of irregular waves over a mound. *Journal of Waterway*, *Port*, *Coastal and Ocean Engineering* 1989; **115**(2):269–284.

DOI: 10.1002/fld